Supplementary Information

Extraordinary Phase Transition Revealed in a van der Waals Antiferromagnet

Xiaoyu Guo[1, Δ] , Wenhao Liu[2, Δ], Jonathan Schwartz[3], Suk Hyun Sung[3], Dechen Zhang[1], Makoto Shimizu[4,*], Aswin L. N. Kondusamy[2], Lu Li[1], Kai Sun[1], Hui Deng[1], Harald O. Jeschke[5], Igor I. Mazin[6], Robert Hovden[3], Bing Lv[2, +] and Liuyan Zhao[1, +]

[1] *Department of Physics, University of Michigan, Ann Arbor, MI 48019, USA*

[2] *Department of Physics, the University of Texas at Dallas, Richardson, TX 75080, USA*

[3] *Department of Materials Science and Engineering, University of Michigan, Ann Arbor, MI 48109, USA*

[4] *Department of Physics, Okayama University, Okayama 700-8530, Japan*

[5] *Research Institute for Interdisciplinary Science, Okayama University, Okayama 700-8530, Japan*

[6] *Department of Physics and Astronomy, and Quantum Science and Engineering Center, George Mason University, Fairfax, VA 22030, USA*

[+] Corresponding to: blv@utdallas.edu, lyzhao@umich.edu

[*] Present address: *Department of Physics, Graduate School of Science, Kyoto University, Kyoto 606-8502, Japan*

[Δ] Authors contribute equally

Supplementary Note 1: extensive scanning transmission electron microscopy (STEM) characterization

We checked the robustness of both the stacking sequence and the atomic lattice for CrSBr using scanning transmission electron microscopy (STEM). The wide-range in-plane atomic resolution STEM images rarely show atomic defects (Supplementary Fig. 1a) and the wide-range cross-sectional STEM images consistently show the right overlying stacking between layers (Supplementary Fig. 1b). Therefore, we believe that the crystal structure of CrSBr is robust and that our sample is of high quality.

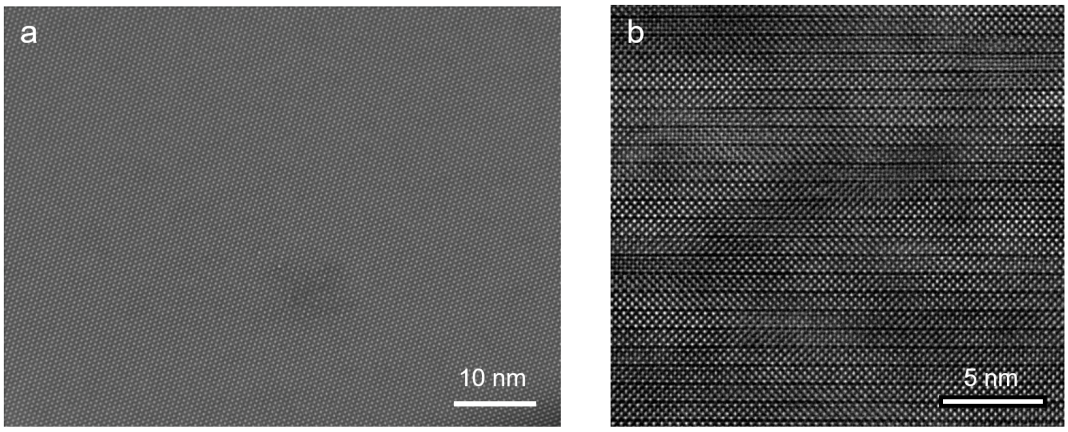

Supplementary Fig. 1 | Extensive STEM characterizations. a. wide-range atomic resolution scanning transmission electron microscopy (STEM) image of CrSBr in the *ab*-plane. **b** Side-view atomic resolution STEM image in the *ac*-plane.

Supplementary Note 2: atomic force microscopy (AFM) characterization

Atomic force microscopy (AFM) captures the surface roughness and atomic steps, with a height resolution of ~ 0.1 nm. Supplementary Fig. 2a shows a representative AFM image taken over a CrSBr sample where we performed second harmonic generation rotational anisotropy (SHG RA) measurements. Over an area of about 130 x 250 μm^2, we only observed a few atomic step sizes of height ~1-2 nm in the lower right corner of a 30 x 55 μm^2 area (see a linecut in Supplementary Fig. 2b). For the rest of the field of view, it is a single atomic terrace with a standard deviation of height to be 0.086 nm (see the histogram of height distribution in Supplementary Fig. 2c). Therefore, our CrSBr single crystals with freshly cleaved surfaces show highly flat surfaces with low density of atomic steps.

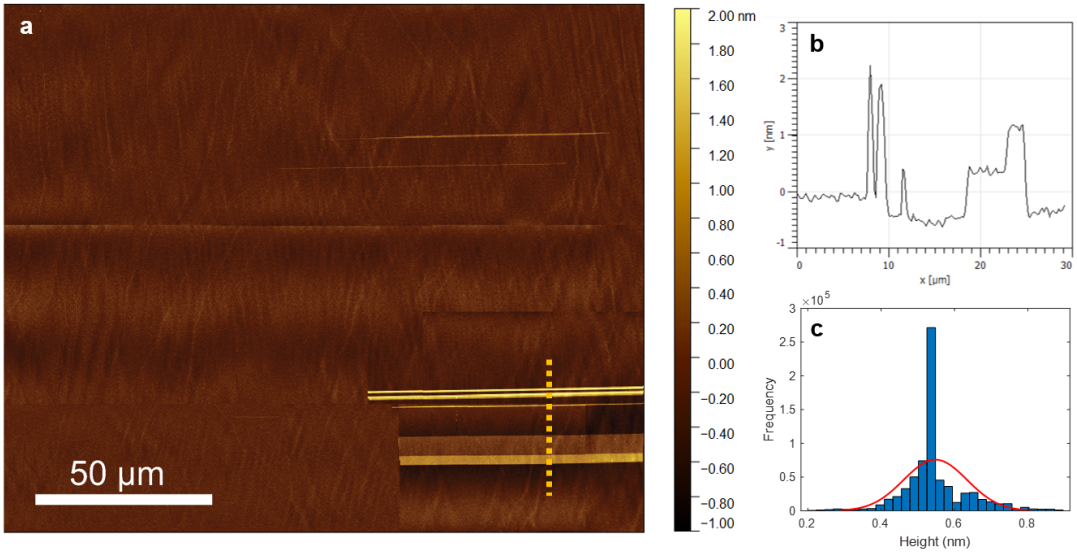

Supplementary Fig. 2 | AFM characterization of CrSBr sample. a. atomic force microscopy (AFM) image taken over a CrSBr sample. **b**. Linecut height profile indicated by the yellow dash line in **a**. **c**. Histogram of height distribution from the flat region. The red curve indicates the Gaussian fit, yielding the standard deviation to be 0.086 nm.

Supplementary Note 3: magnetization measurement of bulk CrSBr

We performed magnetization measurement on the same sample where the SHG RA measurements were performed. As is shown in Supplementary Fig. 3a, apart from the diverging behavior at T_N that indicates the bulk antiferromagnetic (AFM) phase transition, an anomaly is evident at T_F = 30 K, marking the onset of the possible ferromagnetic phase transition. Here, only a weak signature has been observed in our high-quality crystal, consistent with the proposal that this phase transition is related to the magnetic defects inside the crystal. We have also fitted the high temperature (>150 K) magnetic susceptibility using the Curie-Weiss Law:

$$\chi = \chi_0 + \frac{C}{T - T_0}, \tag{1}$$

where χ_0 is the temperature-independent susceptibility arising from the background, C is a constant and T_0 is the Curie-Weiss temperature (Supplementary Fig. 3b). The fitted T_0 = 152 K.

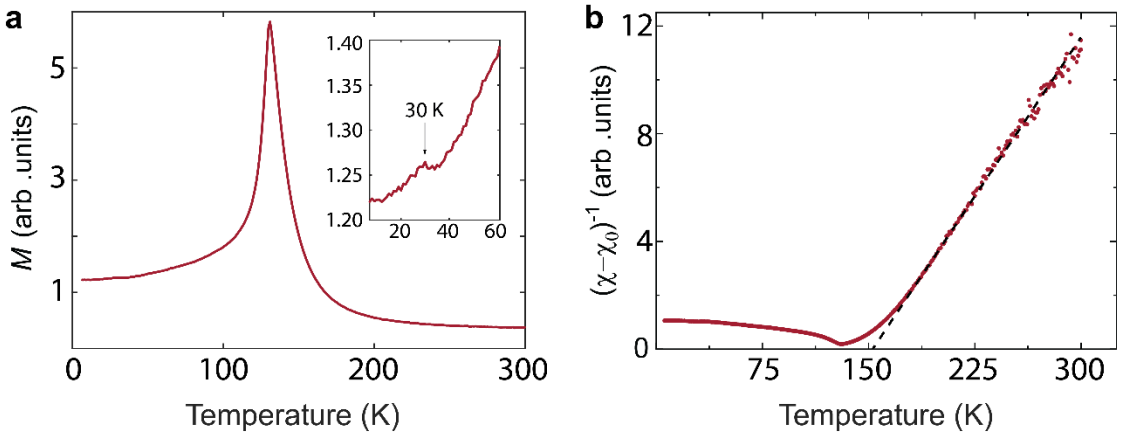

Supplementary Fig. 3 | Magnetization measurement of bulk CrSBr. a, Magnetization measured as a function of temperature. A magnetic field of 1000 Oe was applied along the crystallographic *b*-axis for the measurement. The inset shows the zoom-in region illustrating the anomaly at T_F = 30 K, where the possible ferromagnetic phase transition happens. **b**, Temperature dependence of the inverse magnetic susceptibility. The black dash line shows the fitting of the data using the Curie−Weiss law.

Supplementary Note 4: high temperature oblique SHG RA from bulk CrSBr and SHG radiation source determination

Supplementary Fig. 4 shows the SHG RA patterns measured at 293 K and 185 K on the same sample but at different locations. Both sets of the patterns show the same symmetries: two-fold rotational symmetry about the *c*-axis (C_{2c}), and mirror symmetries with respect to mirrors perpendicular to *a*-axis (m_a) and *b*-axis (m_b), consistent with the crystallography point group *mmm*. They also show similar shapes and SHG intensities. The characteristic temperature scale $T^* = 185$ K that indicates the presence of spin-spin interaction cannot be captured by our SHG RA technique.

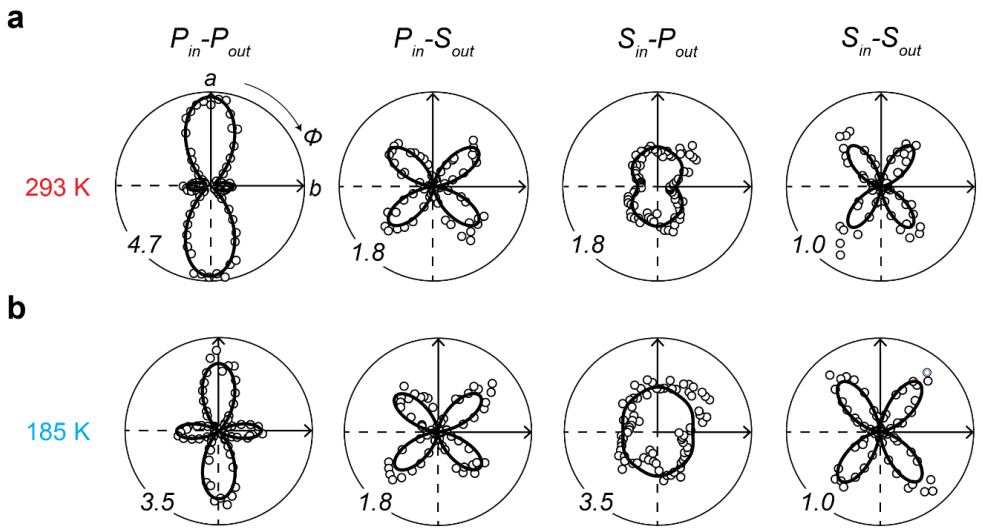

Supplementary Fig. 4 | SHG RA patterns at high temperatures. Four channels of SHG RA patterns measured at **a**, 293 K and **b**, 185 K. Experiment data (circles) are fitted by functional forms simulated based on group theory analysis (solid curves). Numbers at the corners indicate the scales of the polar plots, with 1.0 corresponding to 1 fW.

The experimental data has been fitted with the functional forms simulated from the electric quadrupole (EQ) contribution under the point group *mmm* and shown as solid curves in Supplementary Fig. 4. Other radiation sources including surface electric dipole (ED), bulk magnetic dipole (MD) and electric field induced second harmonic (EFISH) have been ruled out. Supplementary Fig. 5 shows the SHG RA raw data measured at $T = 185$ K, together with the simulated pattens under bulk EQ (point group *mmm*), surface ED (point group *mm2*), bulk MD (point group *mmm*), and EFISH at the surface, with the induced dipole along the *c*-axis (point

group *mmm*), using the functional forms provided. We see that the raw data match the EQ simulation the best. Specifically, in the other three cases, there is always one channel showing no SHG signal, in contrast with our raw data, where SHG signals are present in all four channels. Consequently, we have pinned down bulk EQ as the primary source for our SHG signal.

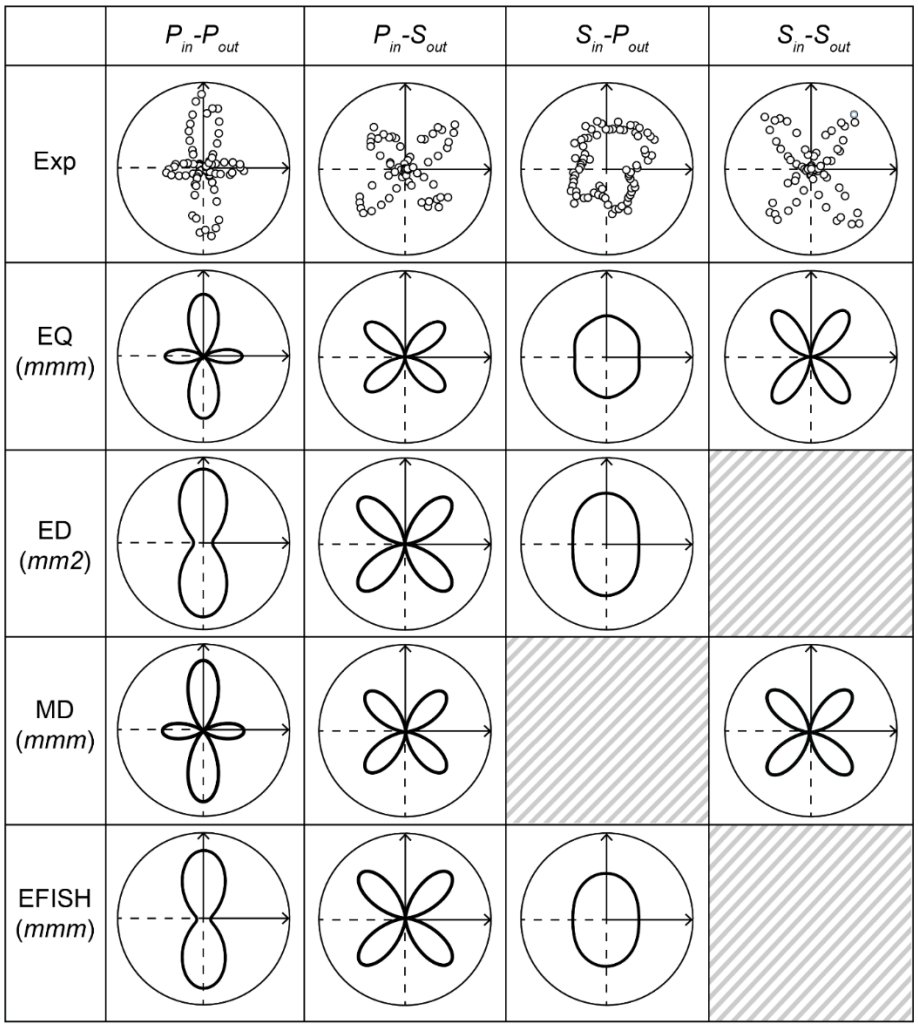

Supplementary Fig. 5 | Simulation results for various SHG radiation sources. SHG RA raw data measured at 185 K in all four channels, together with the simulated pattens from bulk electric quadrupole (EQ), surface electric dipole (ED), bulk magnetic dipole (MD) and electric-field-induced second harmonic (EFISH) at the surface.

Here, we provide the simulated functional forms of the SHG RA patterns at the high temperature from different radiation sources under the corresponding point groups that are used to construct Supplementary Fig. 5.

1. **Bulk EQ** under the point group ***mmm***:

The rank-4 nonlinear optical susceptibility tensor has the form:

$$\chi^{EQ}_{mmm} = \begin{pmatrix} \begin{pmatrix} \chi_{xxxx} & 0 & 0 \\ 0 & \chi_{xxyy} & 0 \\ 0 & 0 & \chi_{xxzz} \end{pmatrix} & \begin{pmatrix} 0 & \chi_{xyxy} & 0 \\ \chi_{xxyy} & 0 & 0 \\ 0 & 0 & 0 \end{pmatrix} & \begin{pmatrix} 0 & 0 & \chi_{xzxz} \\ 0 & 0 & 0 \\ \chi_{xxzz} & 0 & 0 \end{pmatrix} \\ \begin{pmatrix} 0 & \chi_{yyxx} & 0 \\ \chi_{yxyx} & 0 & 0 \\ 0 & 0 & 0 \end{pmatrix} & \begin{pmatrix} \chi_{yyxx} & 0 & 0 \\ 0 & \chi_{yyyy} & 0 \\ 0 & 0 & \chi_{yyzz} \end{pmatrix} & \begin{pmatrix} 0 & 0 & 0 \\ 0 & 0 & \chi_{yzyz} \\ 0 & \chi_{yyzz} & 0 \end{pmatrix} \\ \begin{pmatrix} 0 & 0 & \chi_{zzxx} \\ 0 & 0 & 0 \\ \chi_{zxzx} & 0 & 0 \end{pmatrix} & \begin{pmatrix} 0 & 0 & 0 \\ 0 & 0 & \chi_{zzyy} \\ 0 & \chi_{zyzy} & 0 \end{pmatrix} & \begin{pmatrix} \chi_{zzxx} & 0 & 0 \\ 0 & \chi_{zzyy} & 0 \\ 0 & 0 & \chi_{zzzz} \end{pmatrix} \end{pmatrix}, \tag{2}$$

leading to the following functional forms for the radiation.

In the P_{in}-P_{out} channel:

$$\begin{aligned} S^{PP}_{EQ,mmm} = {} & \mathrm{Sin}[\theta]^2(-\chi_{zzzz}\mathrm{Cos}[\theta]\mathrm{Sin}[\theta]^2 - \mathrm{Cos}[\theta]^3(\chi_{zxzx}\mathrm{Cos}[\phi]^2 \\ & + \chi_{zyzy}\mathrm{Sin}[\phi]^2) + 2\mathrm{Cos}[\theta]\mathrm{Sin}[\theta]^2(\chi_{zzxx}\mathrm{Cos}[\phi]^2 \\ & + \chi_{zzyy}\mathrm{Sin}[\phi]^2))^2 \\ & + \mathrm{Cos}[\theta]^2(2\mathrm{Cos}[\theta]^2\mathrm{Sin}[\theta](\chi_{xxzz}\mathrm{Cos}[\phi]^2 + \chi_{yyzz}\mathrm{Sin}[\phi]^2) \\ & - \mathrm{Sin}[\theta]^3(\chi_{xzxz}\mathrm{Cos}[\phi]^2 + \chi_{yzyz}\mathrm{Sin}[\phi]^2) \\ & - \mathrm{Cos}[\theta]^2\mathrm{Sin}[\theta](\chi_{xxxx}\mathrm{Cos}[\phi]^4 + (2\chi_{xxyy} + \chi_{xyxy} + \chi_{yxyx} \\ & + 2\chi_{yyxx})\mathrm{Cos}[\phi]^2\mathrm{Sin}[\phi]^2 + \chi_{yyyy}\mathrm{Sin}[\phi]^4))^2. \end{aligned} \tag{3}$$

In the P_{in}-S_{out} channel:

$$\begin{aligned} S^{PS}_{EQ,mmm} = {} & (2(\chi_{xxzz} - \chi_{yyzz})\mathrm{Cos}[\theta]^2\mathrm{Cos}[\phi]\mathrm{Sin}[\theta]\mathrm{Sin}[\phi] - (\chi_{xzxz} \\ & - \chi_{yzyz})\mathrm{Cos}[\phi]\mathrm{Sin}[\theta]^3\mathrm{Sin}[\phi] - \mathrm{Cos}[\theta]^2\mathrm{Sin}[\theta]((\chi_{xxxx} \\ & - \chi_{yxyx} - 2\chi_{yyxx})\mathrm{Cos}[\phi]^3\mathrm{Sin}[\phi] + (2\chi_{xxyy} + \chi_{xyxy} \\ & - \chi_{yyyy})\mathrm{Cos}[\phi]\mathrm{Sin}[\phi]^3))^2. \end{aligned} \tag{4}$$

In the S_{in}-P_{out} channel:

$$S_{EQ,mmm}^{SP} = \mathrm{Cos}[\theta]^2\mathrm{Sin}[\theta]^2(\chi_{\mathrm{zyzy}}\mathrm{Cos}[\phi]^2 + \chi_{\mathrm{zxzx}}\mathrm{Sin}[\phi]^2)^2 + \mathrm{Cos}[\theta]^2\mathrm{Sin}[\theta]^2(\chi_{\mathrm{xyxy}}\mathrm{Cos}[\phi]^4 + (\chi_{\mathrm{xxxx}} - 2(\chi_{\mathrm{xxyy}} + \chi_{\mathrm{yyxx}}) + \chi_{\mathrm{yyyy}})\mathrm{Cos}[\phi]^2\mathrm{Sin}[\phi]^2 + \chi_{\mathrm{yxyx}}\mathrm{Sin}[\phi]^4)^2. \quad (5)$$

In the S_{in}-S_{out} channel:

$$S_{EQ,mmm}^{SS} = \mathrm{Sin}[\theta]^2((\chi_{\mathrm{xyxy}} + 2\chi_{\mathrm{yyxx}} - \chi_{\mathrm{yyyy}})\mathrm{Cos}[\phi]^3\mathrm{Sin}[\phi] + (\chi_{\mathrm{xxxx}} - 2\chi_{\mathrm{xxyy}} - \chi_{\mathrm{yxyx}})\mathrm{Cos}[\phi]\mathrm{Sin}[\phi]^3)^2, \quad (6)$$

where θ is the incident polar angle and ϕ the azimuth angle between the scattering plane and the crystallographic *a*-axis.

2. **Surface ED** under the point group $\boldsymbol{mm2}$ and ***i*-type surface ED** under the magnetic point group $\boldsymbol{m'm2'}$:

The rank-3 nonlinear optical susceptibility tensor has the form:

$$\chi_{mm2}^{ED} = \begin{pmatrix} \begin{pmatrix} 0 \\ 0 \\ \chi_{\mathrm{xxz}} \end{pmatrix} & \begin{pmatrix} 0 \\ 0 \\ 0 \end{pmatrix} & \begin{pmatrix} \chi_{\mathrm{xxz}} \\ 0 \\ 0 \end{pmatrix} \\ \begin{pmatrix} 0 \\ 0 \\ 0 \end{pmatrix} & \begin{pmatrix} 0 \\ 0 \\ \chi_{\mathrm{yyz}} \end{pmatrix} & \begin{pmatrix} 0 \\ \chi_{\mathrm{yyz}} \\ 0 \end{pmatrix} \\ \begin{pmatrix} \chi_{\mathrm{zxx}} \\ 0 \\ 0 \end{pmatrix} & \begin{pmatrix} 0 \\ \chi_{\mathrm{zyy}} \\ 0 \end{pmatrix} & \begin{pmatrix} 0 \\ 0 \\ \chi_{\mathrm{zzz}} \end{pmatrix} \end{pmatrix}, \quad (7)$$

leading to the following functional forms for the radiation.

In the P_{in}-P_{out} channel:

$$S_{ED,mm2}^{PP} = 4\mathrm{Cos}[\theta]^4\mathrm{Sin}[\theta]^2\left(\chi_{\mathrm{xxz}}\mathrm{Cos}[\phi]^2 + \chi_{\mathrm{yyz}}\mathrm{Sin}[\phi]^2\right)^2 + \mathrm{Sin}[\theta]^2\left(\chi_{\mathrm{zzz}}\mathrm{Sin}[\theta]^2 + \mathrm{Cos}[\theta]^2\left(\chi_{\mathrm{zxx}}\mathrm{Cos}[\phi]^2 + \chi_{\mathrm{zyy}}\mathrm{Sin}[\phi]^2\right)\right)^2. \quad (8)$$

In the P_{in}-S_{out} channel:

$$S_{ED,mm2}^{PS} = 4\left(\chi_{xxz} - \chi_{yyz}\right)^2 \mathrm{Cos}[\theta]^2 \mathrm{Cos}[\phi]^2 \mathrm{Sin}[\theta]^2 \mathrm{Sin}[\phi]^2. \quad (9)$$

In the S_{in}-P_{out} channel:

$$S_{ED,mm2}^{SP} = \mathrm{Sin}[\theta]^2 (\chi_{zyy} \mathrm{Cos}[\phi]^2 + \chi_{zxx} \mathrm{Sin}[\phi]^2)^2. \quad (10)$$

In the S_{in}-S_{out} channel:

$$S_{ED,mm2}^{SS} = 0. \quad (11)$$

3. **Bulk MD** under the point group ***mmm***:

The rank-3 nonlinear optical susceptibility tensor has the form:

$$\chi_{mmm}^{MD} = \begin{pmatrix} \begin{pmatrix} 0 \\ 0 \\ 0 \end{pmatrix} & \begin{pmatrix} 0 \\ 0 \\ \chi_{xyz} \end{pmatrix} & \begin{pmatrix} 0 \\ \chi_{xyz} \\ 0 \end{pmatrix} \\ \begin{pmatrix} 0 \\ 0 \\ \chi_{yxz} \end{pmatrix} & \begin{pmatrix} 0 \\ 0 \\ 0 \end{pmatrix} & \begin{pmatrix} \chi_{yxz} \\ 0 \\ 0 \end{pmatrix} \\ \begin{pmatrix} 0 \\ \chi_{zxy} \\ 0 \end{pmatrix} & \begin{pmatrix} \chi_{zxy} \\ 0 \\ 0 \end{pmatrix} & \begin{pmatrix} 0 \\ 0 \\ 0 \end{pmatrix} \end{pmatrix}, \quad (12)$$

leading to the following functional forms for the radiation.

In the P_{in}-P_{out} channel:

$$S_{MD,mmm}^{PP} = 4\mathrm{Cos}[\theta]^2 \mathrm{Sin}[\theta]^2 (\mathrm{Cos}[\theta]^4 + \mathrm{Sin}[\theta]^4)(\chi_{yxz} \mathrm{Cos}[\phi]^2 - \chi_{xyz} \mathrm{Sin}[\phi]^2)^2. \quad (13)$$

In the P_{in}-S_{out} channel:

$$S_{MD,mmm}^{PS} = (\chi_{xyz} + \chi_{yxz} - \chi_{zxy})^2 \mathrm{Cos}[\theta]^4 \mathrm{Sin}[\theta]^2 \mathrm{Sin}[2\phi]^2. \quad (14)$$

In the S_{in}-P_{out} channel:

$$S_{MD,mmm}^{SP} = 0. \quad (15)$$

In the S_{in}-S_{out} channel:

$$S^{SS}_{MD,mmm} = \chi^2_{zxy}\mathrm{Sin}[\theta]^2\mathrm{Sin}[2\phi]^2. \tag{16}$$

4. **EFISH** with induced electric dipole along the *c*-axis under the point group ***mmm***:

The rank-4 nonlinear optical susceptibility tensor has the form:

$$\chi^{EFISH}_{mmm} \tag{17}$$
$$= \left\{ \begin{array}{ccc} \begin{pmatrix} \chi_{xxxx} & 0 & 0 \\ 0 & \chi_{xxyy} & 0 \\ 0 & 0 & \chi_{xxzz} \end{pmatrix} & \begin{pmatrix} 0 & \chi_{xyxy} & 0 \\ \chi_{xxyy} & 0 & 0 \\ 0 & 0 & 0 \end{pmatrix} & \begin{pmatrix} 0 & 0 & \chi_{xzxz} \\ 0 & 0 & 0 \\ \chi_{xxzz} & 0 & 0 \end{pmatrix} \\ \begin{pmatrix} 0 & \chi_{yyxx} & 0 \\ \chi_{yxyx} & 0 & 0 \\ 0 & 0 & 0 \end{pmatrix} & \begin{pmatrix} \chi_{yyxx} & 0 & 0 \\ 0 & \chi_{yyyy} & 0 \\ 0 & 0 & \chi_{yyzz} \end{pmatrix} & \begin{pmatrix} 0 & 0 & 0 \\ 0 & 0 & \chi_{yzyz} \\ 0 & \chi_{yyzz} & 0 \end{pmatrix} \\ \begin{pmatrix} 0 & 0 & \chi_{zzxx} \\ 0 & 0 & 0 \\ \chi_{zxzx} & 0 & 0 \end{pmatrix} & \begin{pmatrix} 0 & 0 & 0 \\ 0 & 0 & \chi_{zzyy} \\ 0 & \chi_{zyzy} & 0 \end{pmatrix} & \begin{pmatrix} \chi_{zzxx} & 0 & 0 \\ 0 & \chi_{zzyy} & 0 \\ 0 & 0 & \chi_{zzzz} \end{pmatrix} \end{array} \right\},$$

leading to the following functional forms for the radiation.

In the P_{in}-P_{out} channel:

$$\begin{aligned} S^{PP}_{EFISH,mmm} = {} & 4\mathrm{Cos}[\theta]^4\mathrm{Sin}[\theta]^2(\chi_{xzxz}\mathrm{Cos}[\phi]^2 + \chi_{yzyz}\mathrm{Sin}[\phi]^2)^2 \\ & + \mathrm{Sin}[\theta]^2(\chi_{zzzz}\mathrm{Sin}[\theta]^2 + \mathrm{Cos}[\theta]^2(\chi_{zxxz}\mathrm{Cos}[\phi]^2 \\ & + \chi_{zyyz}\mathrm{Sin}[\phi]^2))^2 \end{aligned} \tag{18}$$

In the P_{in}-S_{out} channel:

$$S^{PS}_{EFISH,mmm} = 4(\chi_{xzxz} - \chi_{yzyz})^2\mathrm{Cos}[\theta]^2\mathrm{Cos}[\phi]^2\mathrm{Sin}[\theta]^2\mathrm{Sin}[\phi]^2 \tag{19}$$

In the S_{in}-P_{out} channel:

$$S^{SP}_{EFISH,mmm} = \mathrm{Sin}[\theta]^2(\chi_{zyyz}\mathrm{Cos}[\phi]^2 + \chi_{zxxz}\mathrm{Sin}[\phi]^2)^2 \tag{20}$$

In the S_{in}-S_{out} channel:

$$S^{SS}_{EFISH,mmm} = 0. \tag{21}$$

Supplementary Note 5: domain survey on bulk CrSBr

We have surveyed several locations on two pieces of bulk CrSBr samples. Supplementary Fig. 6a and 6b present the optical image of the two CrSBr samples. Supplementary Fig. 6c shows the SHG RA patterns measured in the P_{in}-P_{out} channel at the locations numbered and labeled in Supplementary Fig. 6a and 6b. It can be noted that each of the CrSBr sample is a single domain.

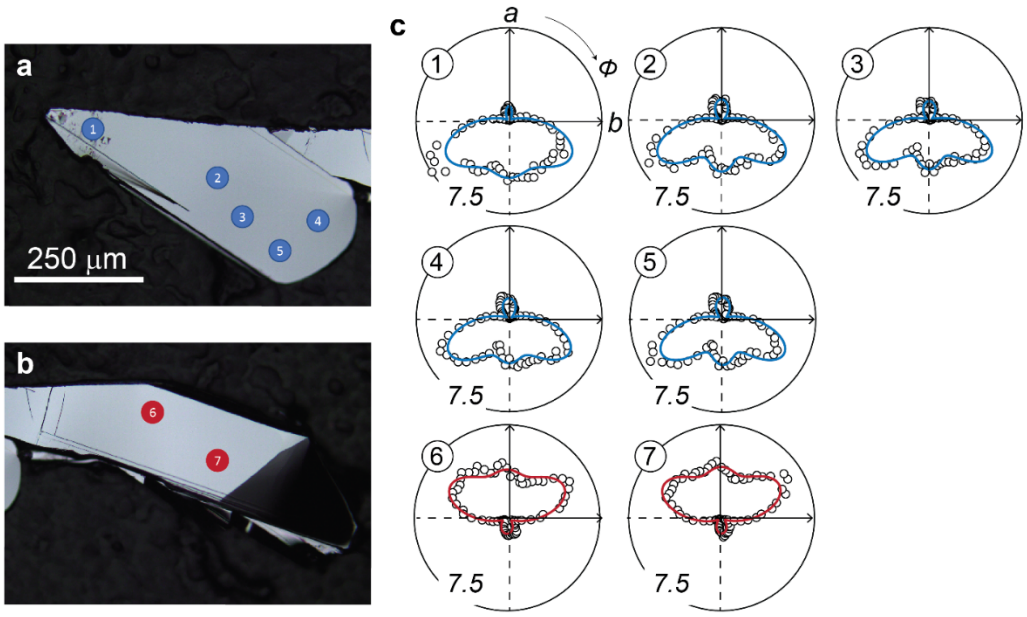

Supplementary Fig. 6 | Spatial survey of magnetic domains of bulk CrSBr. Optical image of **a**, sample 1 and **b**, sample 2. **c**, SHG RA in the P_{in}-P_{out} channel measured at the locations numbered and labelled in **a** and **b**. Experiment data (circles) are fitted by functional forms simulated based on group theory analysis (solid curves). Numbers at the corners indicate the scales of the polar plots, with 1.0 corresponding to 1 fW.

We also surveyed the SHG RA patterns at the same location on the sample through multiple thermal cycles. Supplementary Fig. 7a shows the SHG RA patterns in the four polarization channels observed through the first cool down. After heating up to 185 K (Supplementary Fig. 7b) and cool down to 80 K again, a different set of SHG RA patterns are observed (Supplementary Fig. 7c). The patterns shown in Supplementary Fig. 7a and Supplementary Fig. 7c are related by m_a and C_{2c}, which are the relations between the degenerate magnetic domains. This indicates that different magnetic domains are randomly selected through each thermal cycle. We have performed four thermal cycles, one of which shows the flip of the SHG RA patterns.

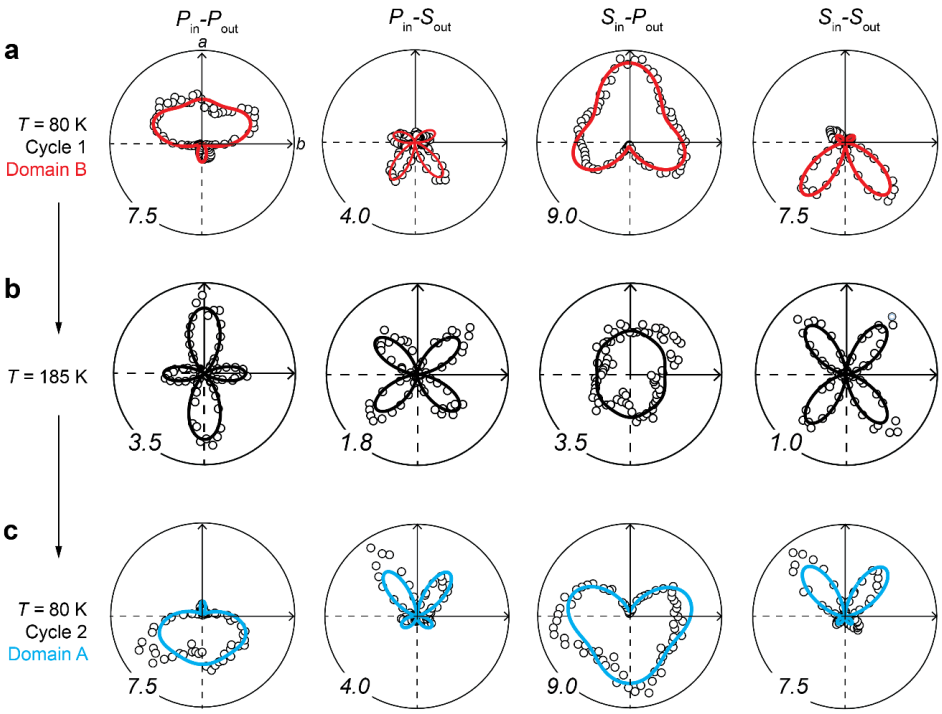

Supplementary Fig. 7 | Magnetic domains of bulk CrSBr under different thermal cycles. SHG RA patterns measured at the same location on the sample through multiple thermal cycles. Two sets of patterns, related by m_a and C_{2c}, have been observed at 80 K, which come from **a**, domain B and **c**, domain A. **b**, SHG RA patterns measured at T = 185 K. Experiment data (circles) are fitted by functional forms simulated based on group theory analysis (solid curves). Numbers at the corners indicate the scales of the polar plots, with 1.0 corresponding to 1 fW.

Supplementary Note 6: superposition of surface ED and bulk EQ

Here, we provide the functional forms of SHG radiation under the superposition of bulk EQ and surface ED. The nonlinear optical susceptibility tensor for bulk EQ has already been given in Supplementary Note 4. We now need to consider the time-variant (*c*-type) SHG radiation from the surface under the magnetic point group $\boldsymbol{m'm2'}$:

The rank-3 nonlinear optical susceptibility tensor has the form:

$$\chi_{m'm2'}^{ED,c,A} = \begin{pmatrix} \begin{pmatrix} \chi_{xxx} \\ 0 \\ 0 \end{pmatrix} & \begin{pmatrix} 0 \\ \chi_{xyy} \\ 0 \end{pmatrix} & \begin{pmatrix} 0 \\ 0 \\ \chi_{xzz} \end{pmatrix} \\ \begin{pmatrix} 0 \\ \chi_{yxy} \\ 0 \end{pmatrix} & \begin{pmatrix} \chi_{yxy} \\ 0 \\ 0 \end{pmatrix} & \begin{pmatrix} 0 \\ 0 \\ 0 \end{pmatrix} \\ \begin{pmatrix} 0 \\ 0 \\ \chi_{zxz} \end{pmatrix} & \begin{pmatrix} 0 \\ 0 \\ 0 \end{pmatrix} & \begin{pmatrix} \chi_{zxz} \\ 0 \\ 0 \end{pmatrix} \end{pmatrix} \tag{22}$$

for domain A, and

$$\chi_{m'm2'}^{ED,c,B} = \begin{pmatrix} \begin{pmatrix} -\chi_{xxx} \\ 0 \\ 0 \end{pmatrix} & \begin{pmatrix} 0 \\ -\chi_{xyy} \\ 0 \end{pmatrix} & \begin{pmatrix} 0 \\ 0 \\ -\chi_{xzz} \end{pmatrix} \\ \begin{pmatrix} 0 \\ -\chi_{yxy} \\ 0 \end{pmatrix} & \begin{pmatrix} -\chi_{yxy} \\ 0 \\ 0 \end{pmatrix} & \begin{pmatrix} 0 \\ 0 \\ 0 \end{pmatrix} \\ \begin{pmatrix} 0 \\ 0 \\ -\chi_{zxz} \end{pmatrix} & \begin{pmatrix} 0 \\ 0 \\ 0 \end{pmatrix} & \begin{pmatrix} -\chi_{zxz} \\ 0 \\ 0 \end{pmatrix} \end{pmatrix} \tag{23}$$

for domain B. Note that the rank-3 nonlinear optical susceptibility tensors for domain A and B are related by a minus sign because of the time-reversal relation, leading to the different interference patterns shown in Figure 4 of the main text. The radiation solely from the ***c*-type surface ED** under the magnetic point group $\boldsymbol{m'm2'}$ is:

In the P_{in}-P_{out} channel:

$$S_{ED,m'm2'}^{PP} = \Big(-2\chi_{zxz}\mathrm{Cos}[\theta]\mathrm{Cos}[\phi]\mathrm{Sin}[\theta]^2 + \mathrm{Cos}[\theta]\Big(\chi_{xzz}\mathrm{Cos}[\phi]\mathrm{Sin}[\theta]^2 + \mathrm{Cos}[\theta]^2\big(\chi_{xxx}\mathrm{Cos}[\phi]^3 + (\chi_{xyy} + 2\chi_{yxy})\mathrm{Cos}[\phi]\mathrm{Sin}[\phi]^2\big)\Big)\Big)^2. \quad (24)$$

In the P_{in}-S_{out} channel:

$$S_{ED,m'm2'}^{PS} = \Big(\chi_{xzz}\mathrm{Sin}[\theta]^2\mathrm{Sin}[\phi] + \mathrm{Cos}[\theta]^2\Big(\big(\chi_{xxx} - 2\chi_{yxy}\big)\mathrm{Cos}[\phi]^2\mathrm{Sin}[\phi] + \chi_{xyy}\mathrm{Sin}[\phi]^3\Big)\Big)^2. \quad (25)$$

In the S_{in}-P_{out} channel:

$$S_{ED,m'm2'}^{SP} = \Big(\mathrm{Cos}[\theta]\big(\chi_{xyy}\mathrm{Cos}[\phi]^3 + \big(\chi_{xxx} - 2\chi_{yxy}\big)\mathrm{Cos}[\phi]\mathrm{Sin}[\phi]^2\big)\Big)^2. \quad (26)$$

In the S_{in}-S_{out} channel:

$$S_{ED,m'm2'}^{SS} = \Big(\big(\chi_{xyy} + 2\chi_{yxy}\big)\mathrm{Cos}[\phi]^2\mathrm{Sin}[\phi] + \chi_{xxx}\mathrm{Sin}[\phi]^3\Big)^2. \quad (27)$$

Note that the SHG radiation from domain A and B share the same form. Only the interference between the surface magnetism and the bulk EQ radiations will lead to distinct patterns between domain A and domain B, as is shown below:

Considering the interference between surface **ED** with surface magnetism under the magnetic point group $\boldsymbol{m'm2'}$ and **EQ** under the point group $\boldsymbol{mmm}$:

In the P_{in}-P_{out} channel:

$$S_{ED+EQ}^{PP} = (\mathrm{Sin}[\theta](-2\chi_{zxz}\mathrm{Cos}[\theta]\mathrm{Cos}[\phi]\mathrm{Sin}[\theta] - \chi_{zzzz}\mathrm{Cos}[\theta]\mathrm{Sin}[\theta]^2 - \mathrm{Cos}[\theta]^3(\chi_{zxzx}\mathrm{Cos}[\phi]^2 + \chi_{zyzy}\mathrm{Sin}[\phi]^2) + 2\mathrm{Cos}[\theta]\mathrm{Sin}[\theta]^2(\chi_{zzxx}\mathrm{Cos}[\phi]^2 + \chi_{zzyy}\mathrm{Sin}[\phi]^2)) + \mathrm{Cos}[\theta](\chi_{xzz}\mathrm{Cos}[\phi]\mathrm{Sin}[\theta]^2 + 2\mathrm{Cos}[\theta]^2\mathrm{Sin}[\theta](\chi_{xxzz}\mathrm{Cos}[\phi]^2 + \chi_{yyzz}\mathrm{Sin}[\phi]^2) - \mathrm{Sin}[\theta]^3(\chi_{xzxz}\mathrm{Cos}[\phi]^2 + \chi_{yzyz}\mathrm{Sin}[\phi]^2) + \mathrm{Cos}[\theta]^2(\chi_{xxx}\mathrm{Cos}[\phi]^3 + (\chi_{xyy} + 2\chi_{yxy})\mathrm{Cos}[\phi]\mathrm{Sin}[\phi]^2) - \mathrm{Cos}[\theta]^2\mathrm{Sin}[\theta](\chi_{xxxx}\mathrm{Cos}[\phi]^4 + (2\chi_{xxyy} + \chi_{xyxy} + \chi_{yxyx} + 2\chi_{yyxx})\mathrm{Cos}[\phi]^2\mathrm{Sin}[\phi]^2 + \chi_{yyyy}\mathrm{Sin}[\phi]^4)))^2. \quad (28)$$

In the P_{in}-S_{out} channel:

$$S_{ED+EQ}^{PS} = (2(\chi_{xxzz} - \chi_{yyzz})\mathrm{Cos}[\theta]^2\mathrm{Cos}[\phi]\mathrm{Sin}[\theta]\mathrm{Sin}[\phi] + \chi_{xzz}\mathrm{Sin}[\theta]^2\mathrm{Sin}[\phi] - (\chi_{xzxz} - \chi_{yzyz})\mathrm{Cos}[\phi]\mathrm{Sin}[\theta]^3\mathrm{Sin}[\phi] + \mathrm{Cos}[\theta]^2((\chi_{xxx} - 2\chi_{yxy})\mathrm{Cos}[\phi]^2\mathrm{Sin}[\phi] + \chi_{xyy}\mathrm{Sin}[\phi]^3) - \mathrm{Cos}[\theta]^2\mathrm{Sin}[\theta]((\chi_{xxxx} - \chi_{yxyx} - 2\chi_{yyxx})\mathrm{Cos}[\phi]^3\mathrm{Sin}[\phi] + (2\chi_{xxyy} + \chi_{xyxy} - \chi_{yyyy})\mathrm{Cos}[\phi]\mathrm{Sin}[\phi]^3))^2. \quad (29)$$

In the S_{in}-P_{out} channel:

$$S_{ED+EQ}^{SP} = (-\mathrm{Cos}[\theta]\mathrm{Sin}[\theta](\chi_{zyzy}\mathrm{Cos}[\phi]^2 + \chi_{zxzx}\mathrm{Sin}[\phi]^2) + \mathrm{Cos}[\theta](\chi_{xyy}\mathrm{Cos}[\phi]^3 + (\chi_{xxx} - 2\chi_{yxy})\mathrm{Cos}[\phi]\mathrm{Sin}[\phi]^2 - \mathrm{Sin}[\theta](\chi_{xyxy}\mathrm{Cos}[\phi]^4 + (\chi_{xxxx} - 2(\chi_{xxyy} + \chi_{yyxx}) + \chi_{yyyy})\mathrm{Cos}[\phi]^2\mathrm{Sin}[\phi]^2 + \chi_{yxyx}\mathrm{Sin}[\phi]^4)))^2. \quad (30)$$

In the S_{in}-S_{out} channel:

$$S_{ED+EQ}^{SS} = ((\chi_{xyy} + 2\chi_{yxy})\mathrm{Cos}[\phi]^2\mathrm{Sin}[\phi] + \chi_{xxx}\mathrm{Sin}[\phi]^3 - \mathrm{Sin}[\theta]((\chi_{xyxy} + 2\chi_{yyxx} - \chi_{yyyy})\mathrm{Cos}[\phi]^3\mathrm{Sin}[\phi] + (\chi_{xxxx} - 2\chi_{xxyy} - \chi_{yxyx})\mathrm{Cos}[\phi]\mathrm{Sin}[\phi]^3))^2 \quad (31)$$

for domain A. Domain B shares the similar functional forms with an additional minus sign before all the rank-3 tensor elements χ_{ijk}.

Supplementary Note 7: thickness dependent SHG measurements

The symmetry analysis discussed in the last section is the primary criterion to distinguish the surface and bulk contributions to SHG. Besides, we performed thickness dependent SHG RA at 80 K as a secondary check to confirm the surface ED SHG origin from the surface AFM order. We investigated three different thickness, 160nm, 450nm, and 7500nm (7.5 μm) that are quantified by the atomic force microscopy measurements. In Supplementary Fig. 8, we show their SHG RA patterns in the S_{in}-S_{out} channel and their decomposition into the bulk EQ and surface ED contributions. We can clearly see that:

a) As the thickness increases, the surface ED SHG contribution stays nearly the same. This is consistent with its surface nature.
b) In contrast, when the thickness increases, the bulk EQ SHG contribution increases which is also consistent with its bulk nature. From the trend, we can also roughly estimate our light penetration depth is slightly deeper than 450nm.

With the confirmation of the surface origin of SHG that onsets at T_s = 140 K, we are confident about our assignment of the surface layered AFM order.

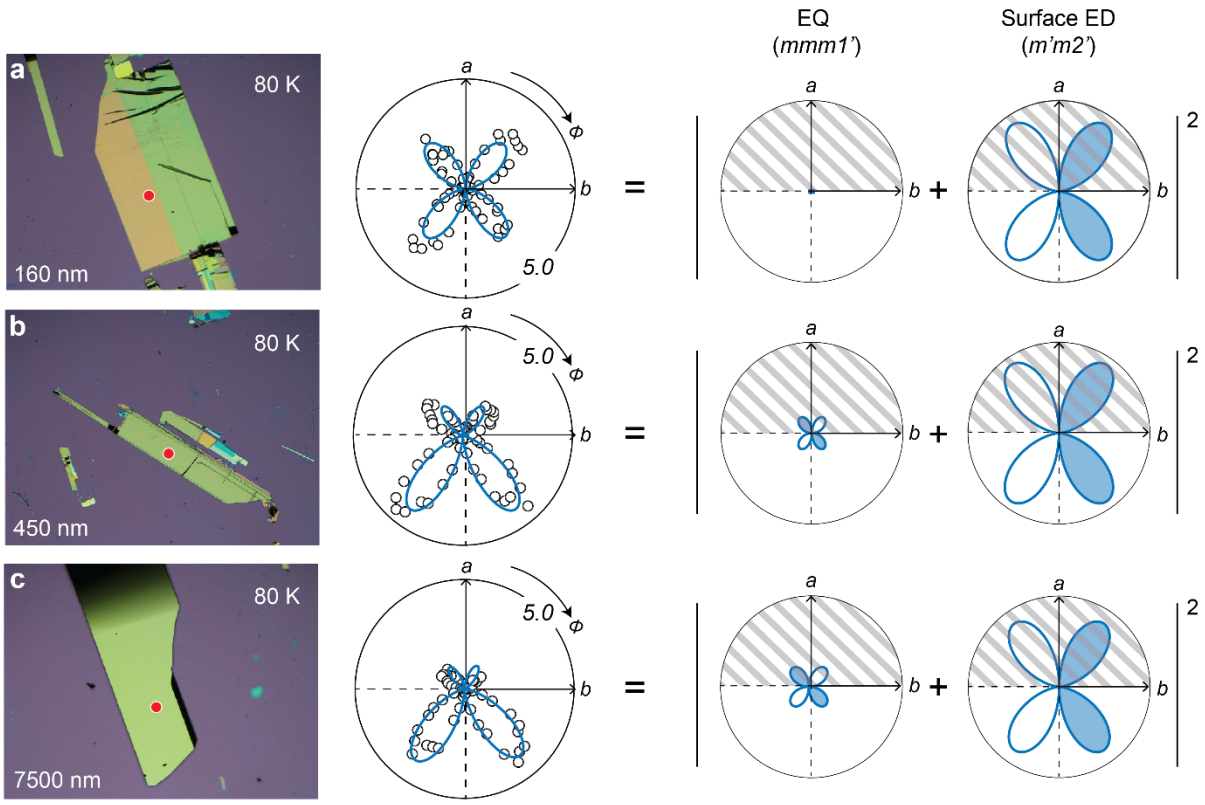

Supplementary Fig. 8 | Thickness dependent SHG RA. Optical image, bulk EQ and surface ED SHG contributions in the S_{in}-S_{out} channel and their interference for samples with thickness **a**. 160 nm **b**. 450 nm and **c**. 7500 nm. All the patterns are measured at 80 K. Red dots in the optical images indicate the location for SHG measurements. Experiment data (circles) are fitted by functional forms simulated based on group theory analysis (solid curves). Numbers at the corners indicate the scales of the polar plots, with 1.0 corresponding to 1 fW. EQ: electric quadrupole, ED: electric dipole.

Supplementary Note 8: SHG RA measured in sequence of time

We prove the stability of our system by showing the consistency of RA SHG data taken at the same temperature but 45 minutes apart. Supplementary Fig. 9 shows four RA SHG patterns taken every 15 min in the P_{in}-P_{out} channel at 130 K. Within our technique sensitivity, there are no observable changes in the measured patterns, indicating the system is in its equilibrium state.

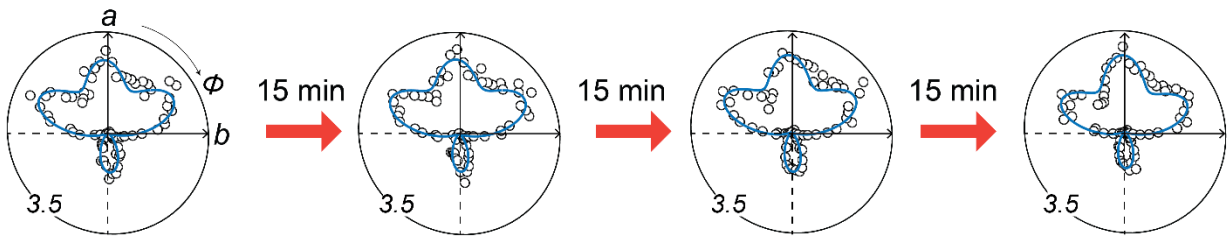

Supplementary Fig. 9 | SHG RA patterns taken every 15 min in the P_{in}-P_{out} channel at 130 K. No observable changes are detected, indicating the system is in its equilibrium state. Experiment data (circles) are fitted by functional forms simulated based on group theory analysis (solid curves). Numbers at the corners indicate the scales of the polar plots, with 1.0 corresponding to 1 fW.

Supplementary Note 9: temperature dependence of C_2^{ED} and D_2^{ED}

The $C_2^{ED} = \chi_{xxx}$ and $D_2^{EQ} = \chi_{xyxy} + 2\chi_{yyxx} - \chi_{yyyy}$ fitted from the temperature-dependent SHG RA in the S_{in}-S_{out} channel are plotted in Supplementary Fig. 10. Both C_2^{ED} and D_2^{EQ} have a relatively large uncertainty. Despite this, D_2^{EQ} is capable of tracking T^{**} and T_S, similar as D_1^{EQ} in the Fig. 5c of the main text. However, unlike D_1^{EQ}, D_2^{EQ} cannot capture T_N due to the larger uncertainty.

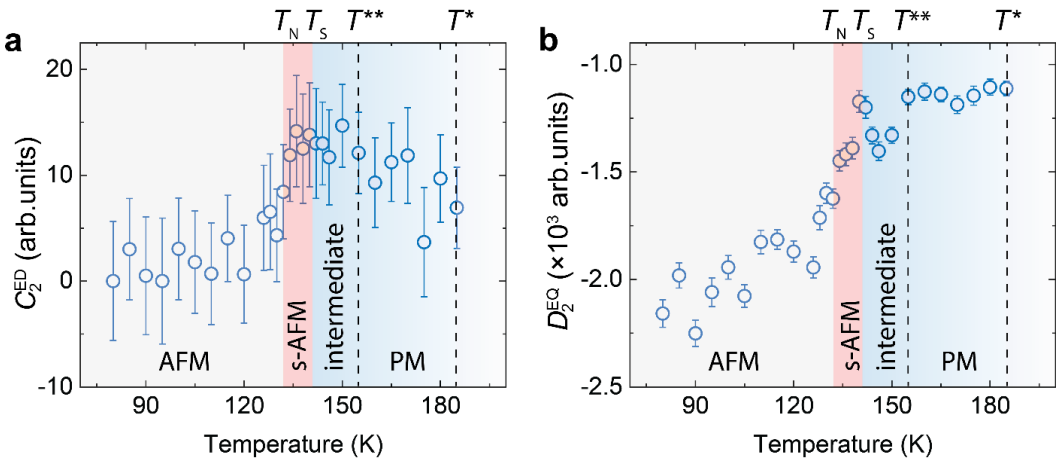

Supplementary Fig. 10 | Temperature dependence of C_2^{ED} and D_2^{EQ}. **a**, C_2^{ED} and **b**, D_2^{EQ} as a function of temperature fitted from the S_{in}-S_{out} channel. The regions of paramagnetism (PM), intermediate magnetic crossover (intermediate), surface antiferromagnetism (s-AFM) and bulk antiferromagnetism (AFM) are shaded in different colors, with their characteristic temperatures marked. Error bars indicate the standard deviations from the fitting.

Supplementary Note 10: SHG and magnetization measurements from multiple samples

We performed the same SHG RA measurements and analysis on a sample prepared separately (referred as Sample 2). We also performed the fit of the temperature dependence of the electric dipole (ED) susceptibility tensor elements, using the functional form of $C_1^{ED} = A\,(T_s - T)^{\beta} + B$ for $T < T_s$ and $C_1^{ED} = B$ for $T \geq T_s$. Due to the kink at T_N = 132 K known as the impact on the surface order by the bulk order, we limit our fit to the data between the temperature range of 132 K – 200 K. For our two independent RA SHG measurements on two samples, the fitted surface onset temperatures are T_S = 140 ± 0.2K (Sample 1, sample for the main text Figure 5) and 140 ± 0.1 K (Sample 2), respectively (see Supplementary Figs. 11a and 11c). The critical exponent, β, varies dramatically between different temperature ranges for fitting, being β = 0.6 ± 0.2 for Sample 1 and 0.4 ± 0.1 for Sample 2. Such a variation in β is due to the lack of data points between 132 K and 140 K and also the impact of the bulk onset at 132 K. The error represents the 95% confidence interval calculated from the standard deviations given by the fitting process. In addition, we note that the temperature dependent ED signals show a notable kink (i.e., change of curvature) near T_N = 132 K for both measurements, which is consistent with the expectation/prediction that the bulk order at T_N = 132 K impacts the surface order.

Furthermore, we performed the temperature dependent magnetization measurements on Sample 1 and another sample from the same batch of Sample 2. For both samples, we can clearly see the bulk transition temperature at T_N = 132 ± 1 K (see Supplementary Figs. 11b and 11d). Our bulk magnetism onset temperature is consistent with the literature values for bulk single crystal CrSBr.

With these results, we are confident about our finding of two phase transitions happening in 3D bulk CrSBr, a surface phase transition at T_S = 140 ± 0.2 K and a bulk ordering onset at T_N = 132 ± 1 K.

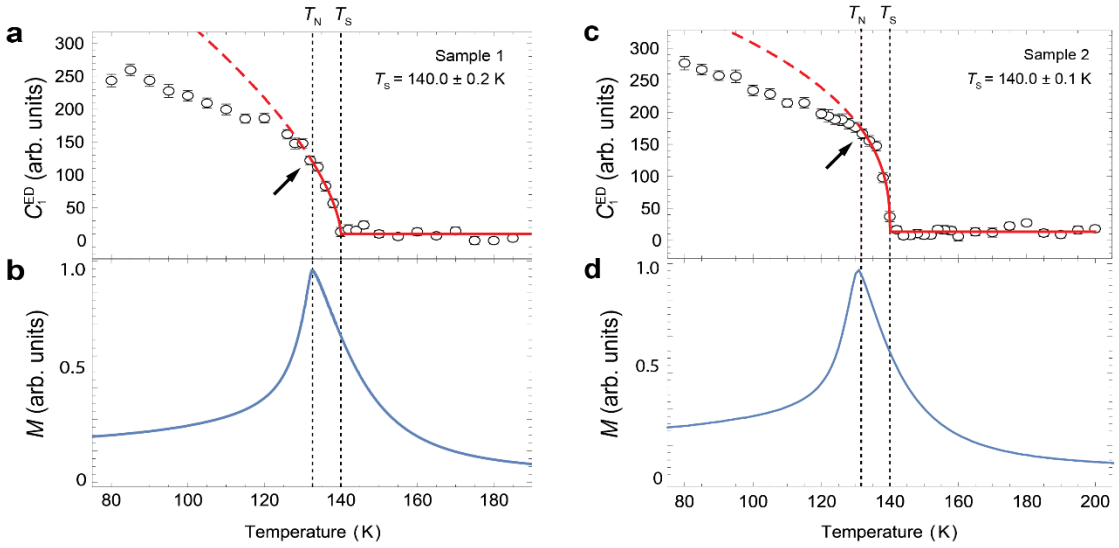

Supplementary Fig. 11 | Observation of enhanced surface magnetic transition temperatures in multiple samples. Surface ED SHG coefficient C_1^{ED} and magnetization M as a function of temperature measured from sample 1 (**a** and **b**) and sample 2 (**c** and **d**). The extracted transition temperatures are also labelled. Red curves show the best order-parameter fit using data for $T > 132$ K. Black arrows indicate the kinks at $T_N = 132$ K. Error bars are standard deviations from the fitting.

Supplementary Note 11: assignment of crossover at the temperature scale T^{**} = 155 K

Our revised interpretation for T^{**} = 155 K is a temperature scale, below which the spin forms fluctuating, short-ranged patches within and between *ab*-planes for the entire bulk. Within each patch, the spins on average align along the *b*-axis direction (Supplementary Fig. 12a). Then, below T_S = 140 K, the surface layers order in the layered AFM state whereas the deeper bulk remains in the fluctuating, short-ranged form (Supplementary Fig. 12b). And finally, below T_N = 132K, the entire sample enters the layered AFM state (Supplementary Fig. 12c). The reasons for this revised assignment are listed as follows:

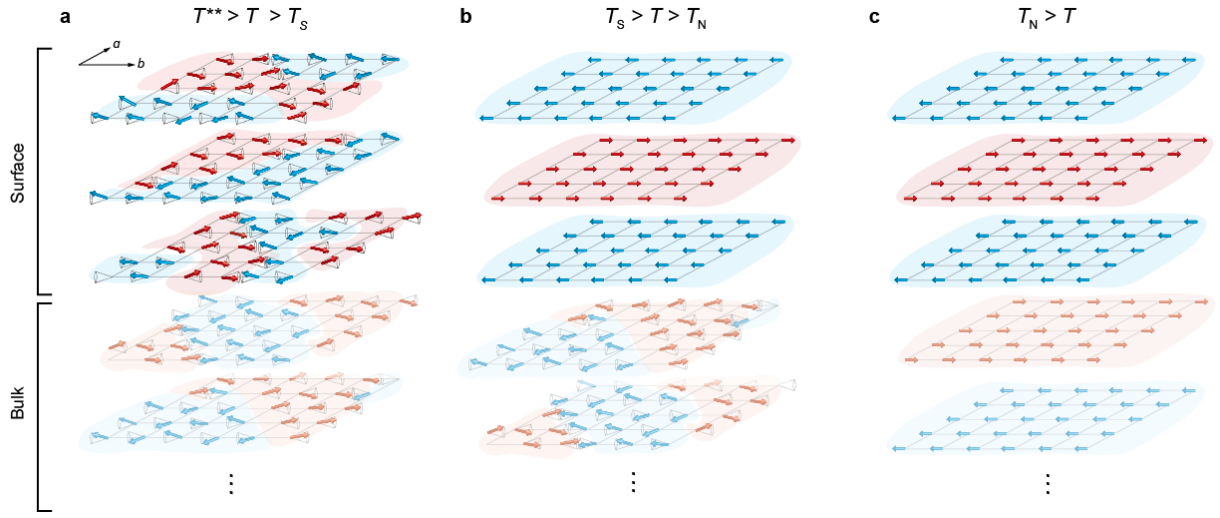

Supplementary Fig. 12 | Proposed spin texture at various temperatures. a. At $T^{**} > T > T_S$ the whole sample develops a multi-patch state with short-range correlations. **b**. At $T_S > T > T_N$, the surface develops layered AFM order, whereas the bulk still only has short-range correlations. **c**. $T < T_N$, a long-range layered AFM order is developed across the sample.

1) We observed both T^{**} = 155 K and T_S = 140 K, in addition to T_N = 132 K, in the temperature dependent SHG RA data (Figures 5b and 5c of the main text). If the spins form the ferromagnetic long-range order within the *ab*-plane below T^{**} = 155 K, we can ask what changes in SHG RA would be upon the formation of this state. From the symmetry perspective, the surface magnetic point group of this *c*-axis incoherent magnetic state is *m'm2'*, and the bulk magnetic point group is *mmm1'*. Due to the in-plane long-range order, we would anticipate the surface ED contribution and the bulk EQ contribution to SHG RA right below T^{**} = 155K. In addition, due to the *c*-axis incoherence, its surface magnetic state has 2^N options,

where N is the layer number for surface magnetism, and therefore we would expect 2^N degenerate domain states. However, right below T^{**} = 155 K (above T_S = 140 K), we don't observe surface ED SHG in our data and only find one type of SHG RA between T^{**} and T_S. This distinction between our expectation of SHG RA for the *c*-axis incoherent state and the observed SHG RA between T^{**} and T_S motivates us to consider a different possibility of the magnetic state between T^{**} and T_S from the "intralayer order" with *c*-axis incoherence.

2) At the same time, our proposed picture of fluctuating, short-ranged patches with an average spin alignment along the *b*-axis inside patches is consistent with our experimental data. As there is no global symmetry breaking either at the surface or inside the bulk, we don't observe changes in RA SHG patterns across T^{**}. But because there is an average effect to make the *b*-axis slightly different from the *a*-axis throughout the sample, we do observe in the bulk EQ SHG that the susceptibility tensor element amplitudes change.
3) We find the transition from the *c*-axis incoherent "intralayer order" to the layered AFM order is unlikely to happen at T_N = 132 K for bulk CrSBr. Between these two states, the energy gain is in the order of $\Delta E \sim nNJ$, where J is the interlayer AFM exchange coupling, n is the number of interlayer bond per two neighboring layers, and N is the number of layers for a bulk sample. And between these two states, the entropy reduction is $\Delta S \sim k_B N \ln 2$, as the number of possible states reduces from 2^N to 2. A thermodynamic phase transition can happen when $\Delta E = T_c \Delta S$, leading to a critical temperature of $T_c = \frac{nJ}{k_B}$. For the intralayer long range orders, $n \to \infty$ and therefore $T_c \to \infty$, rather than the finite temperature of T_N = 132 K. Therefore, it is unlikely that the bulk magnetic state is the *c*-axis incoherent "intralayer order" below 155 K.

With these considerations, we assign the observed temperature scale of T^{**} = 155 K to be a crossover temperature scale for the system to enter a state with fluctuating, short-ranged patches of spins that on average align with the *b*-axis within individual patches.

Supplementary Note 12: supplementary results from density functional theory (DFT) calculation

Supplementary Fig. 13 shows the U-dependence of J_6, which hardly changes from bulk to monolayer CrSBr under various settings.

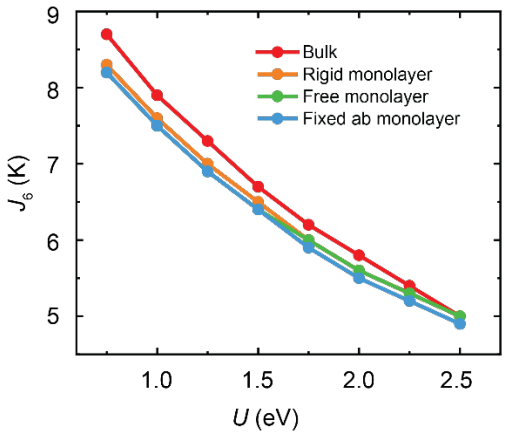

Supplementary Fig. 13 | U-dependence of J_6 for bulk CrSBr (red), rigid monolayer (orange), fixed *ab* monolayer (blue) and free monolayer (green).

Supplementary Table 1 provides the information from J_1 to J_7 and the Curie-Weiss temperatures in bulk CrSBr and monolayer CrSBr under various settings. The corresponding Cr-Cr distance for each J has also been provided.

Supplementary Table 1. Energy mapping results for CrSBr bulk and monolayers

bulk

U (eV)	J_1	J_2	J_3	J_4	J_5	J_6	J_7	ϑ_{CW}
0.75	-7.7(8)	-37.7(7)	-31.7(3)	-0.4(7)	0.2(7)	8.7(4)	-2.4(2)	278.1
1.0	-12.1(7)	-38.9(6)	-30.2(3)	-0.4(6)	0.1(6)	7.9(4)	-2.3(2)	293.8
1.25	-15.8(6)	-39.9(5)	-28.7(3)	-0.5(5)	0.1(5)	7.3(3)	-2.3(2)	306.1
1.5	-19.1(6)	-40.6(5)	-27.3(2)	-0.5(5)	0.1(5)	6.7(3)	-2.3(2)	315.9
1.75	-21.9(5)	-41.1(4)	-26.0(2)	-0.5(4)	0.1(4)	6.2(3)	-2.2(2)	323.4
2.0	-24.5(5)	-41.5(4)	-24.8(2)	-0.5(4)	0.1(4)	5.8(2)	-2.2(2)	329.3
2.25	-26.7(4)	-41.7(4)	-23.6(2)	-0.5(4)	0.1(4)	5.4(2)	-2.1(1)	333.9
2.5	-28.7(4)	-41.8(3)	-22.5(2)	-0.5(3)	0.1(3)	5.0(2)	-2.1(1)	337.3
$d_{\mathrm{Cr-Cr}}$ (Å)	3.544	3.592	4.738	5.917	6.166	7.089	7.603	

rigid monolayer

U (eV)	J_1	J_2	J_3	J_4	J_5	J_6	J_7	ϑ_{CW}
0.75	-8.7(8)	-38.7(7)	-31.5(3)	-0.5(7)	-0.1(7)	8.3(4)	-2.4(2)	288.1
1.0	-13.0(7)	-40.0(6)	-30.1(3)	-0.6(6)	-0.1(6)	7.6(4)	-2.3(2)	303.5
1.25	-16.7(6)	-40.9(5)	-28.7(3)	-0.6(5)	-0.1(5)	7.0(3)	-2.3(2)	315.6
1.5	-20.0(6)	-41.6(5)	-27.4(2)	-0.6(5)	-0.1(5)	6.5(3)	-2.2(2)	325.1
1.75	-22.9(5)	-42.1(4)	-26.2(2)	-0.6(4)	-0.1(4)	6.0(3)	-2.2(2)	332.5
2.0	-25.4(5)	-42.5(4)	-25.0(2)	-0.6(4)	0.0(4)	5.6(2)	-2.2(2)	338.0
2.25	-27.7(4)	-42.7(4)	-23.9(29	-0.6(4)	0.0(4)	5.3(2)	-2.1(1)	342.5
2.5	-29.7(4)	-42.8(3)	-22.8(2)	-0.5(3)	0.0(3)	5.0(2)	-2.1(1)	345.8
$d_{\mathrm{Cr-Cr}}$ (Å)	3.544	3.592	4.738	5.917	6.166	7.089	7.603	

free monolayer

U (eV)	J_1	J_2	J_3	J_4	J_5	J_6	J_7	ϑ_{CW}
0.75	-5.4(8)	-40.7(7)	-34.2(3)	-0.8(7)	-0.2(7)	8.2(4)	-2.0(2)	296.8
1.0	-9.9(7)	-41.7(6)	-32.7(3)	-0.8(6)	-0.1(6)	7.5(4)	-1.9(2)	310.9
1.25	-13.8(6)	-42.5(5)	-31.3(3)	-0.9(5)	-0.1(5)	6.9(3)	-1.9(2)	322.5
1.5	-17.3(6)	-43.0(5)	-29.9(2)	-0.8(5)	-0.1(5)	6.4(3)	-1.9(2)	331.3
1.75	-20.3(5)	-43.4(4)	-28.6(2)	-0.8(4)	0.0(4)	6.0(3)	-1.9(2)	337.5
2.0	-23.0(5)	-43.5(4)	-27.3(2)	-0.7(4)	0.0(4)	5.6(2)	-1.9(2)	342.6
2.25	-25.4(4)	-43.6(4)	-26.2(2)	-0.7(4)	0.1(4)	5.3(2)	-1.9(1)	346.4
2.5	-27.5(4)	-43.5(3)	-25.1(2)	-0.7(3)	0.1(3)	5.0(2)	-1.9(1)	348.8
$d_{\mathrm{Cr-Cr}}$ (Å)	3.533	3.597	4.727	5.901	6.156	7.066	7.591	

fixed ab monolayer

U (eV)	J_1	J_2	J_3	J_4	J_5	J_6	J_7	ϑ_{CW}
0.75	-9.1(8)	-40.1(7)	-34.0(3)	-0.7(7)	-0.1(7)	8.2(4)	-2.1(2)	302.4
1.0	-13.3(7)	-41.2(6)	-32.5(3)	-0.7(6)	-0.1(6)	7.5(4)	-2.0(2)	316.5
1.25	-17.0(6)	-42.0(5)	-31.0(3)	-0.8(5)	-0.1(5)	6.9(3)	-2.0(2)	327.3
1.5	-20.2(6)	-42.6(5)	-29.6(2)	-0.7(5)	-0.1(5)	6.4(3)	-2.0(2)	335.7
1.75	-23.1(5)	-42.9(4)	-28.3(2)	-0.7(4)	-0.1(4)	5.9(3)	-2.0(2)	342.3
2.0	-25.6(5)	-43.1(4)	-27.0(2)	-0.7(4)	0.0(4)	5.5(2)	-2.0(2)	347.0
2.25	-27.9(4)	-43.2(4)	-25.9(2)	-0.7(4)	0.0(4)	5.2(2)	-2.0(1)	350.4
2.5	-29.8(4)	-43.2(3)	-24.7(2)	-0.6(3)	0.1(3)	4.9(2)	-1.9(1)	352.9
$d_{\mathrm{Cr-Cr}}$ (Å)	3.544	3.599	4.738	5.917	6.171	7.089	7.606	

Supplementary Table 2 provides the information of the change in the interatomic distances and bond angles in bulk CrSBr and monolayer CrSBr under different settings.

Supplementary Table 2. Geometrical parameters for the three most important exchange paths of CrSBr

J_1	bulk	fixed ab monolayer	free monolayer	rigid monolayer
Cr-Cr distance (Å)	3.54428	3.54428 (±0%)	3.53296 (-0.32%)	3.54428 (±0%)
Cr-S distance (Å)	2.39300	2.39200 (-0.04%)	2.39051 (-0.10%)	2.39295 (-0.00%)
Cr-S-Cr angle (°)	95.5568	95.6096 (+0.06%)	95.2852 (-0.28%)	95.5596 (-0.00%)
Cr-Br distance (Å)	2.51795	2.52227 (+0.17%)	2.52066 (+0.11%)	2.51800 (+0.00%)
Cr-Br-Cr angle (°)	89.4660	89.2714 (-0.22%)	88.9827 (-0.54%)	89.4634 (-0.00%)

J_2	bulk	fixed ab monolayer	free monolayer	rigid monolayer
Cr-Cr distance (Å)	3.59191	3.59947 (+0.21%)	3.59704 (+0.14%)	3.59182 (-0.00%)
Cr-S distance (Å)	2.40750	2.41018 (+0.11%)	2.40521 (-0.10%)	2.40749 (-0.00%)
Cr-S-Cr angle (°)	96.8750	97.1018 (+0.23%)	97.1894 (+0.32%)	96.8736 (-0.00%)

J_3	bulk	fixed ab monolayer	free monolayer	rigid monolayer
Cr-Cr distance (Å)	4.73800	4.73800 (±0%)	4.72671 (-0.24%)	4.73800 (±0%)
Cr-S distance (Å)	2.40750	2.41018 (+0.11%)	2.40521 (-0.10%)	2.40749 (-0.00%)
Cr-S-Cr angle (°)	159.4781	158.7861 (-0.43%)	158.5902 (-0.56%)	159.4818 (+0.00%)